Available online at www.sciencedirect.com
ScienceDirect
Geochimica et Cosmochimica Acta 74 (2010) 809–817
Geochimica et Cosmochimica Acta
www.elsevier.com/locate/gca

Electrochemically controlled iron isotope fractionation

Jay R. Black [a], Edward D. Young [a,b], Abby Kavner [a,b,*]

[a] Institute for Geophysics and Planetary Physics, University of California, Los Angeles, CA 90095, United States
[b] Earth and Space Sciences, University of California, Los Angeles, CA 90095, United States

Received 24 February 2009; accepted in revised form 27 October 2009; available online 3 November 2009

Abstract

Variations in the stable isotope abundances of transition metals have been observed in the geologic record and trying to understand and reconstruct the physical/environmental conditions that produced these signatures is an area of active research. It is clear that changes in oxidation state lead to large fractionations of the stable isotopes of many transition metals such as iron, suggesting that transition metal stable isotope signatures could be used as a paleo-redox proxy. However, the factors contributing to these observed stable isotope variations are poorly understood. Here we investigate how the kinetics of iron redox electrochemistry generates isotope fractionation. Through a combination of electrodeposition experiments and modeling of electrochemical processes including mass-transport, we show that electron transfer reactions are the cause of a large isotope separation, while mass transport-limited supply of reactant to the electrode attenuates the observed isotopic fractionation. Furthermore, the stable isotope composition of electroplated transition metals can be tuned in the laboratory by controlling parameters such as solution chemistry, reaction overpotential, and solution convection. These methods are potentially useful for generating isotopically-marked metal surfaces for tracking and forensic purposes. In addition, our studies will help interpret stable isotope data in terms of identifying underlying electron transfer processes in laboratory and natural samples.

1. INTRODUCTION

Many transition metal stable isotope signatures appear to be associated with naturally occurring reduction–oxidation (redox) processes (Anbar and Rouxel, 2007). These reactions, involving electron transfer between species, have played an important role in the evolution of the Earth, and help control the cycling of many elements vital for life, including oxygen, carbon, sulfur, and transition metals such as iron (Anbar and Rouxel, 2007; Canfield et al., 2008; Kasting, 2001; Knoll, 2003; Rouxel et al., 2005). Redox-related stable isotope separations in iron have now been observed in a variety of natural and laboratory systems (Johnson et al., 2008), some associated with biological activity (Beard et al., 1999; Brantley et al., 2001; Croal et al., 2004; Crosby et al., 2005, 2007), while isotope partitioning of similar magnitudes due to abiotic processes has also been observed (Anbar, 2004; Anbar et al., 2000; Brantley et al., 2004). Progress in our understanding of the processes that lead to isotope separation, motivated by new developments in our ability to measure stable isotope ratios with high precision, further elucidate the connection between isotope separation and redox state at equilibrium (Anbar et al., 2005; Schauble et al., 2001).

Although the connection between equilibrium isotope fractionation and equilibrium changes in redox state is well established theoretically (Bigeleisen and Mayer, 1947; Urey, 1947), redox reactions often occur away from equilibrium. A combination of stable isotope theory (Bigeleisen, 1949; Young et al., 2002) and electron transfer kinetics (Marcus, 1964, 1965, 1993) suggests that a different isotope fractionation results from electrochemical reactions that occur away from equilibrium, with the fractionation factor equal

* Corresponding author. Address: Institute for Geophysics and Planetary Physics, University of California, Los Angeles, CA 90095, United States.
E-mail addresses: jayblack@ucla.edu (J.R. Black), eyoung@ess.ucla.edu (E.D. Young), akavner@ucla.edu (A. Kavner).

0016-7037/$ - see front matter © 2009 Elsevier Ltd. All rights reserved.
doi:10.1016/j.gca.2009.10.047

to the equilibrium fractionation amplified by a constant proportional to the thermodynamic driving force (Kavner et al., 2005, 2008). This theory is strictly restricted to homogeneous, single-electron-transfer reactions; however, for most redox reactions occurring under real conditions, the electron transfer step is only a single part of a multi-step process, which may also include mass transfer, speciation changes adjacent to the electrode, and phase changes.

The main goal of this study is to use laboratory and theoretical electrochemical tools to examine isotope fractionation arising from distinct reaction steps during a redox reaction: iron electrodeposition. We show experimental evidence demonstrating a large fractionation of iron isotopes arising from the electroplating process that is distinguishable from concurrent and smaller fractionations due to diffusive mass-transport to the electrode. The magnitude of the electrochemical effect observed in the laboratory encompasses the range of observed iron isotope fractionations in nature (Anbar and Rouxel, 2007; Johnson et al., 2008), and so may be useful when linking iron isotope fractionation to natural-world processes which rely upon natural redox gradients such as planetary differentiation (Teng et al., 2008) and the evolution of life (Knoll, 2003). The large and tunable stable isotope signatures produced in electrodeposited metals may provide useful tools for marking and tracing anthropogenic sources of heavy metals for industrial or forensic applications. Further refinement of the theory underlying the electrochemical isotope effect (Kavner et al., 2005, 2008) will allow stable isotope ratios to be used as a tool for investigating the physical chemistry of electrochemical reactions, such as the behavior of electrified interfaces far from equilibrium, and the characterization of solution properties, such as reorganization energies (Marcus, 1993).

2. MATERIALS AND METHODS

A series of potentiostat-based experiments were performed in which iron was electroplated from either iron chloride or iron sulfate plating baths onto a rotating disc electrode and the isotopic composition of the metal deposit analyzed. Experiments were performed as a function of electrode overpotential and rotation rate and in each case a small amount (<0.1%) was plated from ~50 ml aliquots of aqueous plating bath. After each experiment, the plated iron and the remaining solution was collected for isotope analysis using high-resolution mass spectrometry techniques.

2.1. Stock/sample preparation

De-oxygenated stock solutions were prepared by transferring a fixed amount of $FeCl_2{\cdot}2H_2O$ (ACS 99+%) or $FeSO_4{\cdot}7H_2O$ (ACS 99+%) (stored under argon) to a water-jacketed glass cell (cathodic cell) continually degassed with argon (99.9999%). Degassed doubly-distilled water was then injected into the cathodic cell via a septum until 90 ml of solution was obtained. Half this solution was removed via the septum and 30 ml delivered to a secondary anodic cell, 5 ml was used to measure initial sample pH and 10 ml stored in a sample vial to which 1 ml of concentrated HCl (doubly distilled) or H_2SO_4 was added to help prevent oxidation of Fe(II) and precipitation of Fe(III) aqueous species.

Iron chloride samples: Iron plated from 0.8 M $FeCl_2$ stock solutions at pH ~2.5; Temperature = 25 °C.

Iron sulfate samples: Iron plated from 0.46 M $FeSO_4$ + ~0.04 M H_2SO_4 stock solutions at pH ~1.6; Temperature = 25 °C.

Samples of electroplated iron (see Section 2.2 below) from each experiment were dissolved in concentrated HCl (doubly distilled) in Teflon cups. The samples were evaporated down until a sparing amount of solution was left and then the last drop of dissolved iron was diluted with 5 ml of 2% HNO_3 (doubly distilled). Samples were then diluted to a final concentration of 1 ppm for isotopic analyses (see Section 2.3 below).

2.2. Potentiostatic electrodeposition

All samples of iron were electroplated at a constant applied potential relative to a Ag/AgCl double junction reference electrode (filled with 3 m KCl). The applied potential was controlled using an Autolab potentiostat (PGSTAT30) between a glassy carbon Rotating Disc Electrode (RDE, schematic shown in Fig. 1) with a surface area of 7.1 mm^2 and a platinum counter electrode. A two-cell setup was used, with a cathodic half-cell and an anodic half-cell connected via a 2% (w/v) Agar in 4 m KCl or 0.25 M Na_2SO_4

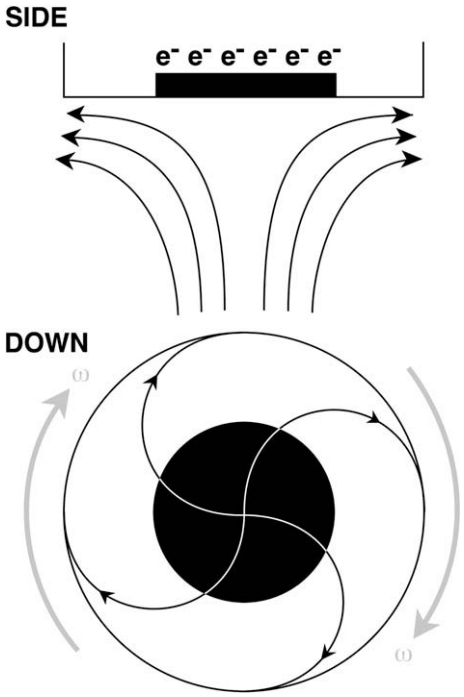

Fig. 1. Rotating disc electrode schematic. Cartoons showing the sideward (SIDE) and downward (DOWN) facing cross-sections of an RDE with fluid flows overlaid (black arrows). The RDE's direction of rotation is shown by the gray arrows. The negatively charged electrode surface (black disc) is shown at the centre of the RDE.

salt bridge (16 × 8 mm i.d.). The electrolyte used in the salt bridge (KCl or Na_2SO_4) was matched with that of the counter-anion in the stock solution to avoid significant changes in the solution chemistry over the course of the experiments. The working and reference electrodes were immersed in ~50 ml of degassed sample solution in the cathodic cell and the temperature of this solution was controlled by an external water bath at 25 °C. The counter electrode was placed in ~30 ml of sample solution in the anodic cell at room temperature. Experiments were run until one Coulomb of charge had been delivered. Other experimental details, such as the average current are presented in Table 1.

To determine if there was any migration of iron across the salt bridge, and whether this induced an isotopic fractionation of iron in the stock solution, samples of each experimental stock were collected before and after an experiment for comparison of their compositions (see Section 2.3).

Experiments were run as a function of overpotential and rotation rate (Table 1). Overpotentials (redox potentials), η, are calculated as the difference between the potential applied at the RDE (V) and the equilibrium potential (V_0) for the iron reduction reaction, measured directly using cyclic voltammetric methods (Bard and Faulkner, 2001). The measured equilibrium potential was in general good agreement with tabulated values. Hydrogen evolution was minimized by working at higher pH than in previous studies (Kavner et al., 2005). Variable iron deposition efficiencies were achieved (1–99%, Table 1), but on average were much greater than those observed by Kavner et al. (2005). No systematic trends are seen in the observed fractionation of plated samples as a function of the deposition efficiency (Table 1).

2.3. MC-ICP-MS analysis

Isotopic analyses were performed using a Thermo-Finnigan Neptune Multi-collector Inductively Coupled Plasma Mass Spectrometer (MC-ICP-MS) housed at UCLA. The instrument is operated at a mass resolving power (instrumental $m/\Delta m$) of ~11,000 (corresponding to a flat-top peak mass resolution of ~3600). We measure $^{56}Fe/^{54}Fe$ and $^{57}Fe/^{54}Fe$ on peak flats corresponding to the three iron ion beams $^{54}Fe^+$, $^{56}Fe^+$, and $^{57}Fe^+$. Molecular interferences from ArN^+, ArO^+, and $ArOH^+$ are avoided by the high mass resolution. A Cetac Aridus® desolvating nebulizer was used (we ran our samples in dry plasma). A standard-sample bracketing technique was used to correct for instrumental mass fractionation. We used an in-house standard, "Spex1" (a standard diluted from a 1000 ppm iron stock), for this purpose. Each analytical session was initiated with zero-enrichments of the standard and in all cases we obtained $0.00 \pm 0.07‰ - 2\sigma$. Samples were analyzed in blocks of 25 cycles with 3–5 standard-bracketed blocks collected per sample. A measurement of the international standard IRMM-14 against Spex 1 was collected before and

Table 1
Summary of electrolysis experiments and MC-ICP-MS results.

Sample	η (V)[a]	Stir rate (rpm)	Average current (mA)	Efficiency (%)[b]	Diffusion limiting current (mA)	$\Delta^{56/54}Fe$ (‰) $\pm 2\sigma$[c]	N[d]
Iron chloride samples:							
FeCl_01	−1.00	1000	−40.32	99	−31.59	−1.21 ± 0.09	5
FeCl_02	−1.00	2500	−43.38	93	−49.94	−1.44 ± 0.08	5
FeCl_03	−1.00	5000	−33.67	95	−70.63	−1.67 ± 0.09	5
FeCl_04	−1.00	10000	−43.10	90	−99.89	−1.71 ± 0.09	5
FeCl_05	−0.50	10000	−11.63	88	−99.89	−1.92 ± 0.08	5
Iron sulfate samples:							
FeSO4_01	−0.50	1000	−1.79	2.8	−31.59	−1.89 ± 0.10	5
FeSO4_02	−0.50	2500	−1.89	1	−49.95	−3.76 ± 0.08	5
FeSO4_03	−0.50	5000	−1.64	1	−70.64	−3.77 ± 0.11	5
FeSO4_04	−0.50	10000	−2.02	0.9	−99.90	−3.64 ± 0.10	5
FeSO4_05	−0.75	1000	−5.50	6	−31.59	−2.36 ± 0.14	5
FeSO4_06	−1.00	500	−7.16	19	−22.34	−1.72 ± 0.18	5
FeSO4_07	−1.00	1000	−8.55	18	−31.59	−1.83 ± 0.09	5
FeSO4_08	−1.00	1000	−10.64	20	−31.59	−1.70 ± 0.09	5
FeSO4_09	−1.00	2500	−10.82	8.6	−49.95	−2.07 ± 0.12	5
FeSO4_10	−1.00	5000	−11.60	1.6	−70.64	−2.41 ± 0.13	5
FeSO4_11	−1.00	10000	−11.05	3.4	−99.90	−2.78 ± 0.11	5
FeSO4_12	−1.50	1000	−19.80	25	−31.59	−1.72 ± 0.10	5
FeSO4_13	−2.00	1000	−27.86	29	−31.59	−1.76 ± 0.09	5
FeSO4_14	−2.00	5000	−35.46	15	−70.64	−2.20 ± 0.09	5
FeSO4_15	−2.00	10000	−30.40	8.9	−99.90	−2.52 ± 0.09	5

[a] Overpotential, η, $(V - V_0)$ relative to measured V_0 from CV spectra.
[b] Percentage yield of metal plated (measured using AAS or ICP-MS) relative to the theoretical mass expected from 1 Coulomb charge delivered.
[c] The isotopic composition of the samples is expressed as a per-mil deviation from the stock solution: $\Delta^{56/54}Fe_{solid-aqueous} = \delta^{56/54}Fe_{solid\ sample} - \delta^{56/54}Fe_{aqueous\ stock}$, where $\delta^{56/54}Fe_{Sample} = [(^{56}Fe/^{54}Fe)_{Sample}/(^{56}Fe/^{54}Fe)_{Spex1} - 1] \times 1000$.
[d] N, number of replicate measurements.

after the sample blocks as a monitor of the efficacy of the mass-fractionation correction.

The experiments were designed to have a constant isotope composition in the reservoir, and in all experiments the isotopic composition of the stock solution before and after an experimental run remain unchanged within the analytical resolution. This also implies that the presence of the salt bridge did not induce any isotope fractionation in the plating solution due to migration. Isotope fractionation of the plated iron samples are reported with respect to the measured aqueous stock solution composition (reported in Table 1). The three-isotope relationships, $\delta^{56/54}Fe_{solid-aqueous}$ vs. $\delta^{57/54}Fe_{solid-aqueous}$, of both the iron sulfate and iron chloride data (details in Table 2) show that the iron isotope behavior is mass-dependent.

3. RESULTS

Iron has four naturally abundant stable isotopes: ^{54}Fe (5.845%), ^{56}Fe (91.754%), ^{57}Fe (2.119%) and ^{58}Fe (0.282%) (Lide, 2007–2008). By convention, the composition of natural samples is reported as a ratio of a heavy (^{56}Fe, ^{57}Fe or ^{58}Fe) to the lightest stable isotope (^{54}Fe) in a sample compared to a standard in a delta notation, or the deviation in per-mil from a standard:

$$\delta^{56/54}Fe_{Sample} = \left(\frac{(^{56}Fe/^{54}Fe)_{Sample}}{(^{56}Fe/^{54}Fe)_{Standard}} \right) \times 1000. \quad (1)$$

Here, we also report ratios in the metallic deposits with reference to the aqueous starting material using a capital delta notation:

$$\Delta^{56/54}Fe_{solid-aqueous} = \delta^{56/54}Fe_{solid\ sample} - \delta^{56/54}Fe_{aqueous\ stock} \quad (2)$$

Our experiments show that in all cases light isotopes of iron are preferentially electroplated, with $\Delta^{56/54}Fe_{solid-aqueous}$ ranging from $\sim -1‰$ to $-3.75‰$ (Fig. 2A, Table 1). The observed isotope fractionations tend to decrease at higher overpotentials (as the reaction is driven far from equilibrium), and also tend to increase with faster rotation rates. The sensitivity of the fractionation to rotation rate increases at larger overpotentials. The largest fractionations are observed at the lowest overpotential, $\eta = -0.5$ V, and are a weak function of rotation rate. Three-isotope systematics (Table 2) demonstrate that fractionation in these experiments followed a mass-dependent process, with a fitted slope in $\delta^{56}Fe$ vs. $\delta^{57}Fe$ space (0.680) very close to that of calculated equilibrium mass dependent fractionation (slope of 0.678, (Young et al., 2002)). Our laboratory-generated fractionations encompass and surpass the range of observed iron stable isotope fractionations in a variety of laboratory and lab experiments (Anbar and Rouxel, 2007; Johnson et al., 2008).

4. DISCUSSION

Our goal is to determine the isotope-dependent kinetics of the iron reduction reaction. Since this reaction involves electron transfer, the isotope-specific reaction rates can be expressed as currents, using the relationship $i = nFAk$, so that

$$^{54}Fe^{2+} + 2e^- \xrightarrow{k_1} {}^{54}Fe_{(s)}, \text{ thus : } {}^{54}i = 2FAk_1$$

$$^{56}Fe^{2+} + 2e^- \xrightarrow{k_2} {}^{56}Fe_{(s)}, \text{ thus : } {}^{56}i = 2FAk_2.$$

Table 2
Iron stable isotope fractionation of electroplated iron on glassy carbon rotating disc electrodes.

Sample	$\delta^{56}Fe$[a] (‰) ± 2σ	$\delta^{57}Fe$[a] (‰) ± 2σ	N[b]	Sample	$\delta^{56}Fe$[a] (‰) ± 2σ	$\delta^{57}Fe$[a] (‰) ± 2σ	N[b]
Iron chloride samples:				*Iron sulfate samples*:			
FeCl_Stk[c]	0.66 ± 0.07	0.96 ± 0.12	5	FeSO4_Stk	0.84 ± 0.08	1.24 ± 0.07	5
FeCl_Cell1[d]	0.646 ± 0.07	0.95 ± 0.09	5	FeSO4_Cell1	0.83 ± 0.06	1.21 ± 0.05	5
FeCl_01	−0.56 ± 0.05	−0.85 ± 0.11	5	FeSO4_Stk	0.84 ± 0.10	1.26 ± 0.19	3
FeCl_02	−0.78 ± 0.04	−1.15 ± 0.09	5	FeSO4_Cell1	0.81 ± 0.04	1.19 ± 0.06	3
FeCl_03	−1.01 ± 0.06	−1.49 ± 0.11	5	FeSO4_01	−1.05 ± 0.05	−1.47 ± 0.06	5
FeCl_04	−1.05 ± 0.06	−1.55 ± 0.16	5	FeSO4_02	−2.93 ± 0.01	−4.29 ± 0.06	5
FeCl_05	−1.26 ± 0.05	−1.86 ± 0.05	5	FeSO4_03	−2.93 ± 0.07	−4.30 ± 0.14	5
				FeSO4_04	−2.81 ± 0.06	−4.13 ± 0.08	5
Standards:				FeSO4_05	−1.52 ± 0.11	−2.26 ± 0.20	5
Spex1	0	0		FeSO4_06	−0.88 ± 0.16	−1.29 ± 0.19	5
IRMM-014	0.219 ± 0.08	0.307 ± 0.12	46	FeSO4_07	−1.00 ± 0.03	−1.48 ± 0.08	5
				FeSO4_08	−0.87 ± 0.04	−1.30 ± 0.11	5
				FeSO4_09	−1.24 ± 0.08	−1.86 ± 0.16	5
				FeSO4_10	−1.58 ± 0.11	−2.34 ± 0.18	5
				FeSO4_11	−1.94 ± 0.08	−2.87 ± 0.09	5
				FeSO4_12	−0.89 ± 0.05	−1.30 ± 0.09	5
				FeSO4_13	−0.93 ± 0.04	−1.35 ± 0.08	5
				FeSO4_14	−1.36 ± 0.04	−2.05 ± 0.13	5
				FeSO4_15	−1.69 ± 0.04	−2.38 ± 0.08	5

[a] The isotopic composition of the samples is expressed as a per-mil deviation from the Spex1 standard using the formula: $\delta^{x}Fe = [(^{x}Fe/^{54}Fe)_{Sample}/(^{x}Fe/^{54}Fe)_{Spex1} - 1] \times 1000$.
[b] N, number of standard bracketed blocks (25 cycles each).
[c] Stk, initial stock solution.
[d] Cell1, final stock solution.

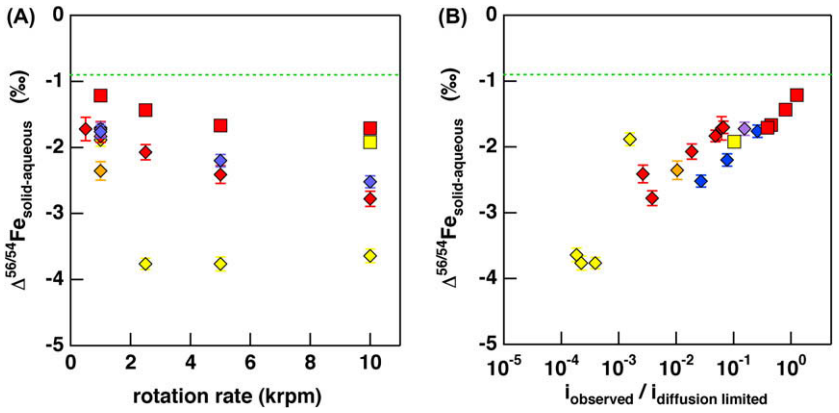

Fig. 2. Iron isotope fractionation in metallic deposits as a function of electrochemical parameters. (A) Isotope fractionation as a function of electrode rotation rate. (B) Isotope fractionation plotted as a function of the ratio of the measured current to diffusion-limited current (see Table 1). Legend: Diamonds: iron plated from iron sulfate solutions; Squares: iron plated from iron chloride solutions; Colors correspond to variable overpotentials: Yellow: −0.5 V; Orange: −0.75 V; Red: −1.0 V; Purple: −1.5 V; Blue: −2.0 V. The dashed green line corresponds to a $\Delta^{56/54}Fe_{solid-aqueous}$ value for the predicted equilibrium fractionation between α-$Fe_{(s)}$-$[Fe(H_2O)_6]^{2+}$ at 25 °C (Schauble et al., 2001). (For interpretation of the references to colour in this figure legend, the reader is referred to the web version of this paper.)

The observed fractionation is related to the currents via the relationship:

$$\delta^{56/54}\mathrm{Fe} = 1000\left(\frac{^{56}i}{^{54}i} - 1\right) \tag{3}$$

(Note: a similar set of relationships can be written for the third isotope system, ^{57}Fe. For the rest of this discussion, we will focus on the data from the ^{56}Fe/^{54}Fe isotope pair. As mentioned before, all of the data fits a mass dependent law.)

Two distinct classes of processes control the flux of material at a charged electrode surface: (1) processes governing mass-transport to the electrode and (2) the chemical and electron transfer steps governing the precipitation reaction at the electrode. Each of these processes may contribute unique stable isotope signatures. The rotating disk electrode experiments allow for control over the relative rates of the two processes. In addition, an isotope fractionation arising from equilibrium considerations is predicted between the bulk solution and the deposited metal. Fig. 3

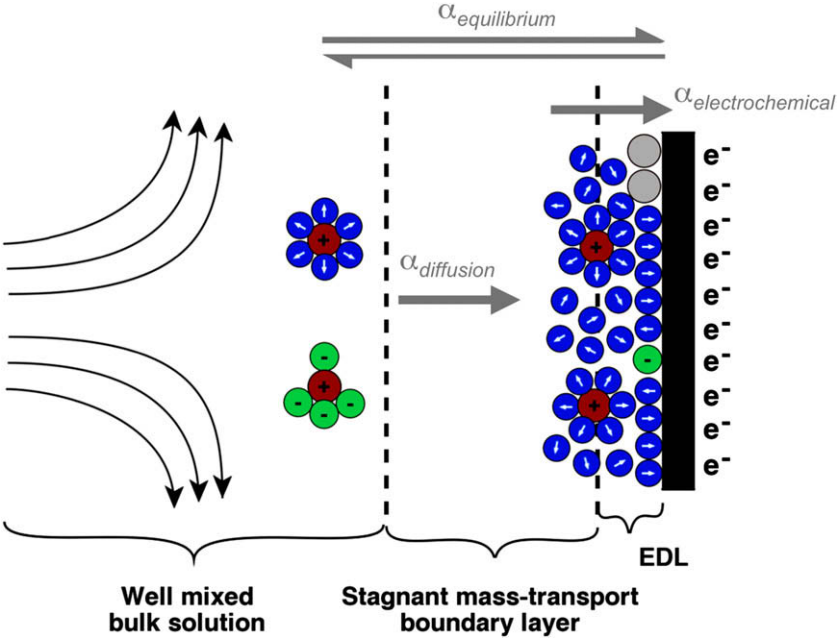

Fig. 3. A cartoon schematic of the microscopic behavior at a negatively charged electrode surface: Initially there are specifically adsorbed species (e.g. water, blue spheres; chloride, green spheres) and aqueous metal complexes (e.g. iron, dark red spheres) at the surface; as charge is transferred an electroplated metal film is deposited (gray spheres) on the electrode and a concentration gradient evolves in the mass-transport boundary layer directly adjacent to the electrode. The processes that may induce an isotopic fractionation across these boundaries (gray arrows across dashed lines, respectively) are labeled as $a_{equilibrium}$, $a_{diffusion}$ and $a_{electrochemical}$ (see text for definitions). EDL stands for the electric double layer. (For interpretation of the references to colour in this figure legend, the reader is referred to the web version of this paper.)

shows a schematic of these microscopic processes taking place at a charged electrode surface and the interaction of ions at this charged interface. In the following sections, we examine the isotope-dependent kinetic behavior of each end-member process, and interpret our experimental observations in terms of these governing processes.

4.1. Flux of iron at the electrode surface

In the absence of mass-transport limitations, the electrodeposition rate far from equilibrium is given by:

$$i_{\text{electrochemical}} = n\text{F}Ak^0 C_{\text{Fe}}(0,t)e^{-\frac{\kappa nF}{RT}\eta} \quad (4)$$

where n is the stoichiometric number of electrons transferred, F is Faraday's constant (96,485 C mol^{-1}), A is the surface area of the electrode (cm^2), k^0 is the standard rate constant (Bard and Faulkner, 2001); $C_{\text{Fe}}(0, t)$ is the concentration of iron (mol cm^{-3}) adjacent the electrode surface at time t (s), κ is the transfer coefficient (Bard and Faulkner, 2001), R is the gas constant (8.3145 J K^{-1} mol^{-1}), T is temperature (K), and η is the overpotential (Volts).

As iron is deposited at the electrode surface a concentration gradient develops in the mass-transport boundary layer adjacent to the charged electrode surface (Fig. 3). The concentration of iron across this boundary layer will be affected by the rate of electrodeposition and the rate by which iron ions are supplied to the electrode surface through convection or diffusion. A schematic of flow velocities at a rotating disc electrode from a sideward and downward perspective (Fig. 1) shows how the rotation produces a cylindrically-symmetric convective flow which supplies iron ion rich fluid to the electrode surface. As the electrode rotation rate increases, the flux of material to the electrode surface is enhanced. The solution of the convective-diffusion equation for a rotating disk electrode (Bard and Faulkner, 2001; Gregory and Riddiford, 1956) provides the flux of a given aqueous species towards the electrode surface as a function of rotation rate, ω. The current induced by this flux reaches a threshold value when the concentration of the aqueous species being deposited on the electrode surface approaches zero. When $C_{\text{Fe}}(0, t) = 0$, this diffusion limiting threshold current is defined by the Levich equation (Gregory and Riddiford, 1956):

$$i_{\text{diffusion limited}} = \left(\frac{0.554}{0.893 + 0.316(D_{\text{Fe}}/\rho)^{0.36}}\right) n\text{F}AD_{\text{Fe}}^{2/3}\rho^{-1/6}\omega^{1/2}C_{\text{Fe}}^{*} \quad (5)$$

where $i_{\text{diffusion limited}}$ is the current (Amps = C s^{-1}); D_{Fe} is the diffusion coefficient of Fe ($\sim 1 \times 10^{-5}$ cm^2 s^{-1}); C_{Fe}^{*} is the concentration of Fe(II) in bulk solution (mol cm^{-3}); ω is the angular velocity of the electrode (s^{-1}); and ρ is the kinematic viscosity of the solution (cm^2 s^{-1}). An increase in the rotation rate of the electrode increases the threshold current above which mass-transport effects dominate (Eq. (5)), and below which electron transfer kinetics dominate (Eq. (4)). Therefore, at low rotation rates, mass transport of material to the electrode is rate-limiting. As the rotation rate increases, enough material is transported to the electrode that the rate of the reaction is dominantly controlled by electron transfer kinetics.

To assess whether this kinetic competition is affecting the outcome of our isotope measurements, we plot isotope fractionation as a function of the ratio of our observed electroplating currents and the calculated diffusion-limiting currents, which are calculated using Eq. (5) and estimates for D_{Fe} (Rodushkin et al., 2004) and ρ (Bard and Faulkner, 2001) (Table 1 and Fig. 2B). Fig. 2B shows that the isotope fractionation displays an almost perfect correlation with the log of this ratio, which varies by several orders of magnitude in these experiments. The largest fractionations occur when the ratio is small—that is, when the actual electrodeposition rate is much lower than the diffusion-limiting rate. When the electroplating current approaches the diffusion-limiting current, the fractionation becomes much smaller.

This result suggests that isotope fractionation, like the overall kinetics, is controlled by a competition between the electrochemical processes at the electrode (which creates large fractionations) and the processes of mass-transport to the electrode (which attenuates the extent of fractionation). In the next section, we discuss models to explain these observations.

4.2. Model of isotope fractionation during electrodeposition

Dauphas and Rouxel (2006) present a reservoir model for fractionation associated with mineral precipitation and diffusion, where fractionation scales linearly between two end member regimes (diffusive control and precipitation controlled fractionation). This model could be used to interpret our data, given a small diffusive fractionation (as measured by Rodushkin et al. (2004)) and a large fractionation associated with the electrodeposition step. Here we present a more detailed model, based in electrochemistry theory, that elaborates on these controls and predicts isotope fractionation from the relationship between underlying electrochemical and diffusion-limiting currents on the overall observed currents (or precipitation rates) in the experiments.

The total observed current (measured average current in each experiment multiplied by electrodeposition efficiency factor, Table 1) is a function of the electrochemical (Eq. (4)) and diffusion limiting (Eq. (5)) currents, as given by the Koutecky–Levich equation (Bard and Faulkner, 2001):

$$\frac{1}{i_{\text{observed}}} = \frac{1}{i_{\text{electrochemical}}} + \frac{1}{i_{\text{diffusion limited}}} \quad (6)$$

Substitution of Eqs. (4) and (5) into Eq. (6) allows for a quantitative evaluation of this model. Fractionation (defined in a delta notation in Eq. (3)) is calculated to be:

$$\begin{aligned}\frac{^{56}i_{\text{observed}}}{^{54}i_{\text{observed}}} &= \frac{1/^{54}i_{\text{electrochemical}} + 1/^{54}i_{\text{diffusion limited}}}{1/^{56}i_{\text{electrochemical}} + {}^{56}i_{\text{diffusion limited}}} \\ &= \frac{1}{\frac{^{54}i_{\text{electrochemical}}}{^{56}i_{\text{electrochemical}}} + \frac{^{54}i_{\text{electrochemical}}}{^{56}i_{\text{diffusion limited}}}} \\ &\quad + \frac{1}{\frac{^{54}i_{\text{diffusion limited}}}{^{56}i_{\text{diffusion limited}}} + \frac{^{54}i_{\text{diffusion limited}}}{^{56}i_{\text{electrochemical}}}}\end{aligned} \quad (7)$$

where:

$$\frac{{}^{54}i_{\text{electrochemical}}}{{}^{56}i_{\text{electrochemical}}} = \frac{{}^{54}k^0}{{}^{56}k^0} e^{({}^{56}\kappa - {}^{54}\kappa)nF\eta/RT} \quad (8)$$

$$\frac{{}^{54}i_{\text{diffusion limited}}}{{}^{56}i_{\text{diffusion limited}}} = \frac{{}^{54}D^{2/3}}{{}^{56}D^{2/3}} \left(\frac{0.893 + 0.316({}^{56}D/\rho)^{0.36}}{0.893 + 0.316({}^{54}D/\rho)^{0.36}} \right) \quad (9)$$

$$\frac{{}^{54}i_{\text{electrochemical}}}{{}^{56}i_{\text{diffusion limited}}} \approx \frac{{}^{56}i_{\text{electrochemical}}}{{}^{54}i_{\text{diffusion limited}}} = \frac{k^0 e^{-\kappa nF\eta/RT}(0.893 + 0.316(D_{Fe}/\rho)^{0.36})}{0.554 D_{Fe}^{2/3} \rho^{-1/6} \omega^{1/2}} \quad (10)$$

where terms which carry a possible mass-dependence are k^0, κ and D_{Fe}. Eq. (7) predicts isotope fractionation arising from a coupled electrochemical/mass-transport process, which can be broken down into an electrochemical term (Eq. (8)), a mass-transport limiting diffusive term (Eq. (9)) and the coupled electrochemical/mass-transport terms (Eq. (10)). The approximation presented in Eq. (10) is only valid far from equilibrium, which our experiments are. Forward models of the behavior of Eq. (7), with variable values for the mass-dependence of each of the three terms independently (D_{Fe}, k^0 and κ) are summarized in Fig. 4A–C.

Fig. 4A shows that using a measured relationship between the diffusion coefficients for isotopes of iron at 20 °C, $D_{54Fe} = 1.000085 \cdot D_{56Fe}$ (Rodushkin et al., 2004), a very small fractionation of −0.056‰ ($\delta^{56/54}$Fe) is produced in the region of diffusive control. This calculation indicates that fractionation of the stable isotopes of iron due to diffusion is insignificant in comparison to the measured fractionations (Table 1). Fractionation by diffusion only also cannot explain our observed changes in fractionation as a function of current ratio (Fig. 2B).

This model is able to take into account an equilibrium-style fractionation between species adjacent to the electrode and the deposited iron. This fractionation can be expressed by considering a mass-dependence of the standard rate constant term (k^0) in Eqs. (4) and (7). Fig. 4B shows how fractionation varies as a function of $i_{\text{observed}}/i_{\text{diffusion limited}}$ due to different values of an equilibrium fractionation between fluid and solid species. The form of this solution does not resemble the trend seen in our results (Fig. 2B); however, large isotope fractionations can arise if the equilibrium isotope fractionation values are large. In a real electroplating system, solution species are likely to vary as a function of distance from the charged electrode due to the electrical double-layer and associated changes in chemical composi-

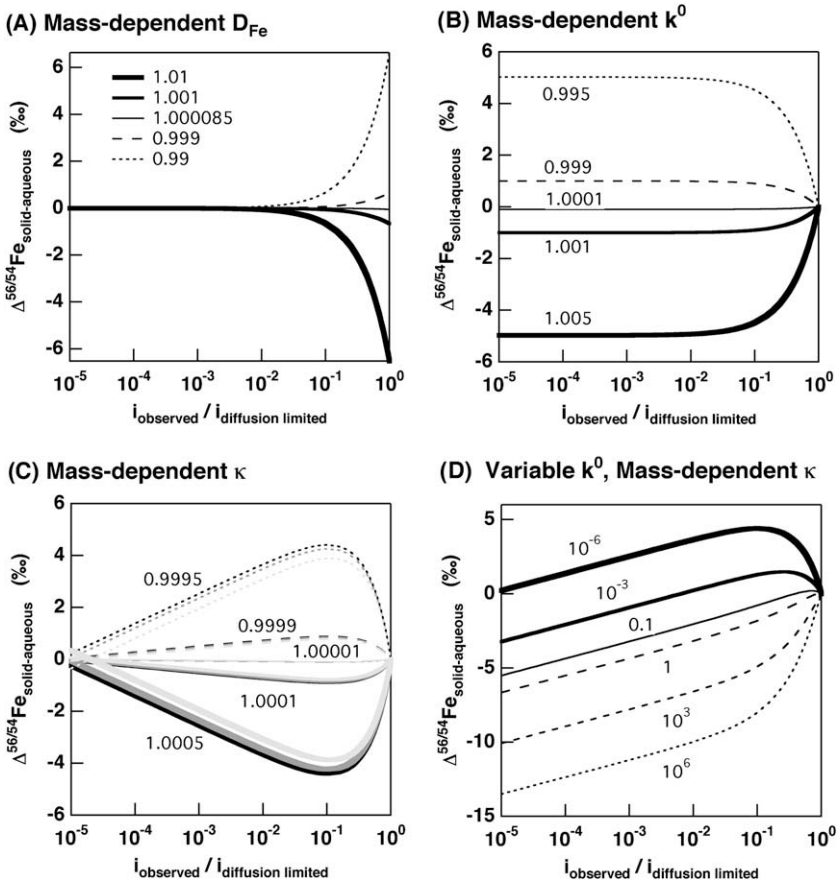

Fig. 4. Independent effects of the mass-dependent variables in Eq. (7) on fractionation as a function of electrochemical and diffusion limiting currents during iron electrodeposition: (A) Variable ${}^{54}D_{\text{Fe}}/{}^{56}D_{\text{Fe}}$ ratios labeled against plotted lines; (B) Variable ${}^{54}\kappa/{}^{56}\kappa$ ratios labeled against plotted lines; (C) Variable ${}^{54}\kappa/{}^{56}\kappa$ ratios labeled against plotted lines, shaded for different RDE rotation rates (10,000, 5000 and 1000 rpm: dark to light shades); (D) Fixed ${}^{54}\kappa/{}^{56}\kappa = 0.9995$ and variable k^0 magnitudes labeled against plotted lines.

tion as the electrode is approached. This may be accompanied by local variations in stable isotope composition. This first-order model does not address this additional reservoir effect; therefore, we will consider the predicted equilibrium stable isotope fractionation between the aqueous iron species in the bulk solution relative to metallic iron as a proxy for the total double-layer behavior. Theoretical studies of aqueous iron complexes predict an equilibrium fractionation factor ($\alpha_{equilibrium}$) resulting in a metal deposit on the electrode that is 0.9‰ lighter than the iron in solution, assuming that the aqueous $[Fe(H_2O)_6]^{2+}$ complex is the aqueous form of iron (Schauble et al., 2001).[1] The extent of this fractionation is considerably smaller than the fractionation observed in our experiments (dashed green lines in Fig. 2). Therefore, although we believe the speciation-induced fractionations may be a part of the story, they likely do not explain our large observed fractionations.

According to our model calculations, the large iron isotope fractionations and the variation with current that are measured in these experiments cannot be explained solely by either diffusion or equilibrium speciation-related fractionation. Clearly, a combination of those two processes also will not yield the trends observed in the data (Fig. 2B). Therefore, we consider a third possible fractionation process arising from a mass-dependent transfer coefficient (κ) in Eqs. (3) and (7). The transfer coefficient describes the shape of the activation energy barrier for charge transfer to take place. By considering a mass-dependence of this term we assume that the activation energy diagram for two different isotopologue systems will be subtly different. This empirical hypothesis is analogous to the outcome of the derivation of the electrochemical isotope effect arising from Marcus theory, as discussed in detail by Kavner et al. (2005, 2008), Fig. 4C plots the predicted fractionation produced at various $^{56}\kappa/^{54}\kappa$ ratios. The first observation is that large fractionations are predicted even from very small mass-dependent deviations in this value (~4‰ fractionations arising from mass dependences of 0.5‰). This emphasizes the ability of the isotope behavior to amplify small mass-dependencies in the reaction energy-coordinate surface, as predicted by Kavner et al. (2005, 2008). Fig. 4D shows that the absolute (non-mass-dependent) value of the standard rate constant k^0 also plays a role in the expression of the isotope fractionation arising from mass-dependent kappa, and that trends representative of the results reported here (Fig. 2B) can be produced from a mass dependent kappa alone (with a corresponding high k^0), without any overprinted mass-dependent equilibrium or diffusive fractionation.

[1] In the bulk solution the speciation of the iron chloride stock solutions, calculated using thermodynamic properties for ferrous chloride species (Parkhurst, 1995), shows that the $[Fe(H_2O)_6]^{2+}_{(aq)}$ complex is predominant (80%) with some coexisting $[FeCl]^{+}_{(aq)}$ (20%). Both species are positively charged and are likely to be attracted to and interact with the negatively charged electrode surface. The speciation in iron sulfate solutions is a little more complicated with three species forming at pH 1.6: $[Fe(H_2O)_6]^{2+}_{(aq)}$ (36.7%), $[FeSO_4]^{0}_{(aq)}$ (50.8%) and $[FeHSO_4]^{+}_{(aq)}$ (12.5%).

5. CONCLUSIONS

While many first-order questions of electrochemical kinetics have been worked out in the extensive and broad field of physical electrochemistry, the isotope effects are not as well elucidated, neither experimentally nor theoretically. With these experiments, we show that two processes—mass-transport to the electrode and the reaction at the electrode—compete to control of the overall kinetics of deposition, and also to determine the overall isotope effect. We show that the isotope effect from mass-transport is much smaller than the isotope effect that occurs during the electron transfer step. We also show that isotopic signatures during electroplating can be controlled over a wide range by varying the experimental conditions. The ability to tune the isotopic composition of metal deposits opens the door for industrial marking and tracing applications.

Our results and modeling help bolster an hypothesis that electron transfer can create large isotope fractionations (Kavner et al., 2005, 2008). The isotope observations can be used to test hypothesis of chemical behavior at an electrified interface and possibly used as a tool for measuring the reorganization energy of electron-transfer reactions. Accurate measurement of such quantities would require an understanding of the mechanism of charge transfer at the electrode surface, including what surface species form, in order to quantify fractionation using a reservoir model.

The experiments are an analog for naturally occurring redox processes in which diffusive and electron transfer mechanisms both contribute to isotope fractionation. In addition to the application to isotope fractionation during redox processes, our experimental approach is also relevant for a wide variety of geochemically relevant applications involving the thermodynamics and kinetics of heterogeneous precipitation. The electrochemical techniques described here allow the mechanisms of isotope fractionation to be investigated in the laboratory as a function of the controlling variables. Ultimately this will allow us to unravel the causes of sensitive isotope signatures observed in nature.

ACKNOWLEDGMENTS

We thank Dr. E. Tonui and Dr. K. Ziegler for technical assistance, and Dr. E. Schauble and Dr. J. Boyce for comments. This work was supported by NASA under the Grant NNG05GQ92G: Exobiology and Evolutionary Biology (A.K.).

REFERENCES

Anbar A. D. (2004) Iron stable isotopes: beyond biosignatures. *Earth Planet. Sci. Lett.* **217**, 223–236.

Anbar A. D., Jarzecki A. A. and Spiro T. G. (2005) Theoretical investigation of iron isotope fractionation between $Fe(H_2O)_3^{+6}$ and $Fe(H_2O)_2^{+6}$: implications for iron stable isotope geochemistry. *Geochim. Cosmochim. Acta* **69**, 825–837.

Anbar A. D., Roe J. E., Barling J. and Nealson K. H. (2000) Nonbiological fractionation of iron isotopes. *Science (Washington, DC)* **288**, 126–128.

Anbar A. D. and Rouxel O. (2007) Metal stable isotopes in paleoceanography. *Annu. Rev. Earth Planet. Sci.* **35**, 717–746.

Bard A. J. and Faulkner L. R. (2001) *Electrochemical Methods: Fundamentals and Applications*. John Wiley & Sons, Inc., USA.

Beard B. L., Johnson C. M., Cox L., Sun H., Nealson K. H. and Aguilar C. (1999) Iron isotope biosignatures. *Science (Washington, DC)* **285**, 1889–1892.

Bigeleisen J. (1949) The relative reaction velocities of isotopic molecules. *J. Chem. Phys.* **17**, 675–678.

Bigeleisen J. and Mayer M. G. (1947) Calculation of equilibrium constants for isotopic exchange reactions. *J. Chem. Phys.* **15**, 261–267.

Brantley S. L., Liermann L. and Bullen T. D. (2001) Fractionation of Fe isotopes by soil microbes and organic acids. *Geology* **29**, 535–538.

Brantley S. L., Liermann L. J., Guynn R. L., Anbar A., Icopini G. A. and Barling J. (2004) Fe isotopic fractionation during mineral dissolution with and without bacteria. *Geochim. Cosmochim. Acta* **68**, 3189–3204.

Canfield D. E., Poulton S. W., Knoll A. H., Narbonne G. M., Ross G., Goldberg T. and Strauss H. (2008) Ferruginous conditions dominated later neoproterozoic deep-water chemistry. *Science (Washington, DC, US)* **321**, 949–952.

Croal L. R., Johnson C. M., Beard B. L. and Newman D. K. (2004) Iron isotope fractionation by Fe(II)-oxidizing photoautotrophic bacteria. *Geochim. Cosmochim. Acta* **68**, 1227–1242.

Crosby H. A., Johnson C. M., Roden E. E. and Beard B. L. (2005) Coupled Fe(II)–Fe(III) electron and atom exchange as a mechanism for Fe isotope fractionation during dissimilatory iron oxide reduction. *Environ. Sci. Technol.* **39**, 6698–6704.

Crosby H. A., Roden E. E., Johnson C. M. and Beard B. L. (2007) The mechanisms of iron isotope fractionation produced during dissimilatory Fe(III) reduction by *Shewanella putrefaciens* and *Geobacter sulfurreducens*. *Geobiology* **5**, 169–189.

Dauphas N. and Rouxel O. (2006) Mass spectrometry and natural variations of iron isotopes. *Mass Spectrom. Rev.* **25**, 515–550.

Gregory D. P. and Riddiford A. C. (1956) Transport to the surface of a rotating disc. *J. Chem. Soc.*, 3756–3764.

Johnson C. M., Beard B. L. and Roden E. E. (2008) The iron isotope fingerprints of redox and biogeochemical cycling in modern and ancient earth. *Annu. Rev. Earth Planet. Sci.* **36**, 457–493.

Kasting J. F. (2001) Perspectives: earth history: the rise of atmospheric oxygen. *Science (Washington, DC, US)* **293**, 819–820.

Kavner A., Bonet F., Shahar A., Simon J. and Young E. (2005) The isotopic effects of electron transfer: an explanation for Fe isotope fractionation in nature. *Geochim. Cosmochim. Acta* **69**, 2971–2979.

Kavner A., John S. G., Sass S. and Boyle E. A. (2008) Redox-driven stable isotope fractionation in transition metals: application to Zn electroplating. *Geochim. Cosmochim. Acta* **72**, 1731–1741.

Knoll A. H. (2003) The geological consequences of evolution. *Geobiology* **1**, 3–14.

Lide, D. R. (2007–2008) CRC Handbook of Chemistry and Physics.

Marcus R. A. (1964) Generalization of the activated complex theory of reaction rates. I. Quantum mechanical treatment. *J. Chem. Phys.* **41**, 2614–2623.

Marcus R. A. (1965) Theory of electron-transfer reactions. VI. Unified treatment for homogeneous and electrode reactions. *J. Chem. Phys.* **43**, 679–701.

Marcus R. A. (1993) Electron-transfer reactions in chemistry: theory and experiment (Nobel lecture). *Angewandte Chemie.* **105**, 1161–1172 (See also Angew. Chem. Int. Ed. Engl. (1993) 32(8), 1111–1121).

Parkhurst, D. L. (1995) User's guide to PHREEQC: a computer program for speciation, reaction-path, advective-transport, and inverse geochemical calculations. *Water Resources Div., Geological Survey*, Lakewood, CO, USA.

Rodushkin I., Stenberg A., Andren H., Malinovsky D. and Baxter D. C. (2004) Isotopic fractionation during diffusion of transition metal ions in solution. *Anal. Chem.* **76**, 2148–2151.

Rouxel O. J., Bekker A. and Edwards K. J. (2005) Iron isotope constraints on the Archean and Paleoproterozoic ocean redox state. *Science (Washington, DC, US)* **307**, 1088–1091.

Schauble E. A., Rossman G. R. and Taylor H. P. (2001) Theoretical estimates of equilibrium Fe-isotope fractionations from vibrational spectroscopy. *Geochim. Cosmochim. Acta* **65**, 2487–2497.

Teng F.-Z., Dauphas N. and Helz R. T. (2008) Iron isotope fractionation during magmatic differentiation in Kilauea Iki Lava Lake. *Science (Washington, DC, US)* **320**, 1620–1622.

Urey H. C. (1947) Thermodynamic properties of isotopic substances. *J. Chem. Soc.*, 562–581.

Young E. D., Galy A. and Nagahara H. (2002) Kinetic and equilibrium mass-dependent isotope fractionation laws in nature and their geochemical and cosmochemical significance. *Geochim. Cosmochim. Acta* **66**, 1095–1104.

GLOSSARY

A: surface area of electrode (cm^2)

$C_{Fe}(0,t)$*:* concentration of Fe(II) at the surface of the electrode ($mol\ cm^{-3}$)

C_{Fe}^{*}*:* concentration of Fe(II) in the bulk solution ($mol\ cm^{-3}$)

D_{Fe}*:* diffusion coefficient of Fe(II) ($cm^2\ s^{-1}$)

e: charge of an electron (1.602×10^{-19} Coulombs)

F: Faradays constant (96,485 Coulombs mol^{-1})

$i_{diffusion\text{-}limited}$*:* current flowing under diffusion control when $C_{Fe}(0, t) = 0$ (Amps)

$i_{electrochemical}$*:* current produced during electron-transfer reaction (Amps)

$i_{observed}$*:* measured current (Amps)

k: rate of electron transfer

k^0*:* standard rate constant, when the rates of forward and backward reaction are equal, ie. at equilibrium ($cm\ s^{-1}$)

m: reduced mass of isotopologue species reacting

n: stoichiometric number of electrons transferred in reaction

R: Gas constant ($8.3145\ J\ K^{-1}\ mol^{-1}$)

RDE: Rotating Disc Electrode

T: temperature (K)

V: potential applied at cathode relative to reference electrode (Volts)

V_0*:* equilibrium potential for electrochemical reaction taking place at cathode, relative to reference electrode (Volts)

$\alpha_{electrochemical}$*:* fractionation factor defined by the ratio of electron transfer rates for two isotopologue species

$\alpha_{equilibrium}$*:* fractionation factor for charge-transfer reaction at equilibrium

η*:* overpotential applied at cathode $= V–V_0$ (Volts)

κ*:* transfer coefficient describing the symmetry of the energy barrier for electron-transfer, $\kappa = 0.5$ indicates a perfectly symmetrical energy barrier

λ*:* reorganization energy ($J\ mol^{-1}$)

ρ*:* kinematic viscosity ($cm^2\ s^{-1}$)

ω*:* RDE rotation rate (s^{-1})

Associate editor: James Farquhar